Pre-print Statement for

"Fe_5S_2 identified as a host for sulfur in Earth's core"

Claire C. Zurkowski[a †], Barbara Lavina[b,c], Abigail Case[a], Kellie Swadba[a], Stella Chariton[b], Vitali B. Prakapenka[b], Andrew J. Campbell[a]

[a]The University of Chicago, Department of the Geophysical Sciences, 5734 S Ellis Ave, Chicago, IL 60637, USA
[b]Center for Advanced Radiation Sources, The University of Chicago, 9700 South Cass Avenue, Lemont, IL 60439, USA
[c]X-ray Science Division, Advanced Photon Source, Argonne National Laboratory, Lemont, IL 60439, USA
[†]Now at Earth and Planets Laboratory, Carnegie Institution for Science, 5251 Broad Branch Road, NW, Washington, DC 20015, USA

Corresponding Author: Claire Zurkowski, czurkowski@carnegiescience.edu

Dear Earth Arxiv,

This manuscript is a non-peer reviewed preprint submitted to *EarthArXiv*. It has been submitted for peer review at *Nature Geoscience.*

Sincerely,
Claire Zurkowski

Fe_5S_2 identified as a host for sulfur in Earth's core

Claire C. Zurkowski[a †], Barbara Lavina[b,c], Abigail Case[a], Kellie Swadba[a], Stella Chariton[b], Vitali B. Prakapenka[b], Andrew J. Campbell[a]

[a]The University of Chicago, Department of the Geophysical Sciences, 5734 S Ellis Ave, Chicago, IL 60637, USA
[b]Center for Advanced Radiation Sources, The University of Chicago, 9700 South Cass Avenue, Lemont, IL 60439, USA
[c]X-ray Science Division, Advanced Photon Source, Argonne National Laboratory, Lemont, IL 60439, USA
[†]Now at Earth and Planets Laboratory, Carnegie Institution for Science, 5251 Broad Branch Road, NW, Washington, DC 20015, USA

Corresponding Author: Claire Zurkowski, czurkowski@carnegiescience.edu

Abstract

Planetary habitability, as we experience on Earth, is linked to a functioning geodynamo which is in part driven by the crystallization of the liquid iron-nickel-alloy core as a planet cools over time. Cosmochemical considerations suggest that sulfur is a candidate light alloying element in rocky planetary cores of varying sizes and oxidation states; such that, iron sulfide phase relations at extreme conditions contribute to outer core thermochemical convection and inner core crystallization in a wide range of planetary bodies. Here we experimentally investigate the structural properties of the Fe-S system and report the discovery of the sulfide, Fe_5S_2, crystallizing in equilibrium with iron at Earth's outer core pressures and high temperatures. Using single-crystal X-ray diffraction techniques, Fe_5S_2 was determined to adopt the complex Ni_5As_2-type structure ($P6_3cm$, $Z = 6$). These results conclude that Fe_5S_2 is likely to crystallize at the interface of Earth's core and mantle and will begin to crystallize during the freezing out of Earth and Venus' core overtime. The increased metal-metal bonding measured in Fe_5S_2 compared to the other high *P-T* iron sulfides may contribute to signatures of higher conductivity from regions of Fe_5S_2 crystallization. Fe_5S_2 could serve as a host for Ni and Si as has been

observed in the related meteoritic phase, perryite, $(Fe, Ni)_8(P, Si)_3$, adding intricacies to elemental partitioning during inner core crystallization. The stability of Fe_5S_2 presented here is key to understanding the role of sulfur in the multicomponent crystallization sequences that drive the geodynamics and dictate the structures of Earth and rocky planetary cores.

Introduction

Earth and the other terrestrial planets along with rocky exoplanets that continue to be discovered are composed of silicate mantles and iron-rich metallic cores (e.g. Birch 1952; Scott and Wasson 1975; Jephcoat and Olsen 1987; Mcdonough and Sun 1995; Rubie et al. 2011). The likelihood of planetary habitability as we know it demands the presence of a geomagnetic field, sustained by a convecting metallic liquid core, that protects the planet from harmful cosmic rays (e.g. Buffet, 2000). In Earth's liquid outer core, the presence of light alloying elements introduces complex pressure-temperature-dependent melting and crystallization thermodynamics that drives core convection (Fearn and Loper, 1981; Stevenson 1981; 1988; Nimmo 2015). While there remains no method to directly sample Earth's or any terrestrial planetary core, iron meteorites are recognized as relics of the cores of planetesimal building blocks of terrestrial planets, and have long provided insight into the cosmochemically abundant light elements contributing to planetary core dynamics (e.g. Scott and Wasson 1975; Malvin et al. 1984). Of the candidate core-alloying elements such as Si, O, S, C, and H, sulfur is present in nearly all iron meteorites, suggesting that sulfur is a core alloying element in rocky planets with varying sizes, oxidation states, and formation histories (Scott and Wasson 1975; Jones and Drake, 1983; Kruijer et al. 2014). Examination of the structural properties of iron sulfides at high pressures

and temperatures (*P*-*T*) is therefore critical to ascertaining the chemistry and thermodynamics of Earth, terrestrial and exoplanetary cores.

At present, the crystallographic assessment of iron sulfides at Earth and planetary core conditions remains limited, even though properties such as density and elasticity are directly related to the atomic arrangement of core-crystallizing phases and are critical for assessing the seismic and dynamic observations of planetary cores. Previous work on Fe-rich systems indicate that tetragonal Fe_3S (Fe_3P-type structure) is stable from Martian core conditions to Earth's outer core conditions (Fei et al. 2000; Kamada et al. 2010; Ozawa et al. 2013; Mori et al. 2017), and an orthorhombic Fe_2S (Co_2Si-type structure) phase becomes stable near Earth's inner-core boundary (ICB) conditions (Tateno et al. 2019). The presence of Si has also been observed to stabilize the Fe_2(S, Si) chemistry over Fe_3S at Mercurian core-mantle-boundary (CMB) conditions (Tao and Fei 2021). These reports were predominantly based powder X-ray diffraction studies at high pressures and temperatures and chemical analyses of recovered samples. However, recent work has demonstrated that the iron-sulfur phase diagram is more complex at high *P*-*T*, but that this complexity requires a superior method for accurately characterizing crystal structures at extreme conditions. Using single-crystal X-ray diffraction techniques on multigrain samples, Co_2P-type Fe_2S (*Pnma*, $Z = 4$) was recently identified and characterized at 90 GPa (Zurkowski et al. *in press*). It remains, however, that these methods have not been applied to iron-sulfide phases synthesized at high temperatures above 90 GPa, leaving the role of sulfur in the crystallization sequences occurring in Venus, Earth and larger rocky exoplanets open to further discovery.

Results and Discussion

In the current study, Fe-rich Fe-S compositions were probed using both single-crystal and powder X-ray diffraction techniques in a laser-heated diamond anvil cell to 200 GPa and 3300 K. At high temperatures between 120 and 200 GPa, spanning Earth's CMB to mid-outer-core conditions, crystallization of hcp-Fe (Figure 1a) is observed in the diffraction patterns along with diffuse streaks and sets of closely spaced reciprocal nodes (Figure 1a, Figure S1), suggesting a complex atomic arrangement of the coexisting sulfide. Upon temperature quenching in this pressure range, diffraction images were collected while rotating the DAC across a +/- 17–30º range (depending on the DAC configuration). Grains of a hexagonal lattice were identified in the reciprocal space with indexed parameters: a = 5.979(3) Å, 11.088(6) Å at 140(2) GPa and 3070(180) K (Table S1). Assessment of the systematic absences for the structure factors reduced for this hexagonal sulfide suggests a $P6_3cm$ space group, and structural solution and positional and displacement parameter refinement converged to the Ni_5As_2-type Fe_5S_2 (Z=6) (Table S2, S3; Figure 2) (Oryshchyn et al. 2011). The Ni_5As_2-type Fe_5S_2 is derived from the Pb_5Sb_2 structure (El-Boragy et al. 1970) where the Fe6 site (Table S3) is split about its position and given half occupancy, changing its Wyckoff site from 6c to 12d (Oryshchyn et al. 2011) (Figure 2, Table S3, Appendix A1). Within error, all sites are fully occupied, except the Fe6 site that is ascribed half occupancy (Oryshchyn et al. 2011).

Additionally, two polytypes associated with stacking variations along the c direction were measured at lower temperatures and in stiff pressure media (Table S1). The Fe_5S_2 polytypism is accompanied by observations of diffuse scattering between reciprocal nodes along the c direction (Figure S1), indicating positional disorder as the atoms configure at high temperatures. Analogous polytypes have been reported in related phases such as Pb_5Sb_2 (Saini et al. 1964).

X-ray diffraction from seven heating cycles performed between 100 and 200 GPa and to 3300 K provide insight into the Fe-rich Fe-S phase relations at outer core pressures and to high temperatures. In each heating experiment, temperatures near melting were attained, and lattices of Fe_5S_2 were indexed in the reciprocal space upon quenching. By further probing locations across the thermal gradient of the laser heated spots, additional Fe-sulfides were characterized, offering information on the lower temperature Fe-saturated sulfide crystal chemistries (Table S1, S2). These include the Fe_3P-type Fe_3S (*I*-4, *Z* = 8) phase (Fei et al. 2000; Seagle et al. 2006; Morard et al. 2007; Kamada et al. 2010; Kamada et al. 2012; Thompson et al. 2020), the *C*23 Fe_2S (Co_2P-type, *Pnma*, *Z* = 4) phase, and the *C*37 Fe_2S (Co_2Si-type, *Pnma*, *Z*=4) phase, in lower temperature regions at 119 GPa, 131 GPa, and 140 GPa, respectively (Figure 3; Table S1, S2). Notably, identification and crystal-structure analysis of Fe_5S_2 and Fe_3S in these Fe-saturated experiments clarifies that Fe_5S_2, not Fe_3S is stable on the solidus above 120 GPa, despite reports from previous powder diffraction studies (e.g. Kamada et al. 2010; Kamada et al. 2012; Ozawa et al. 2013; Mori et al. 2017).

Comparison of the interatomic distances and coordination environments in the Fe-sulfides observed in this study separates Fe_5S_2 as particularly unique among them. Within an interatomic distance of 2.7 Å (Table S4, Appendix A1-A4), *C*23 and *C*37 Fe_2S consist of Fe sites coordinated only by S, Fe_3S marks an increase in Fe-Fe bonding with Fe surrounded by up to 9 Fe sites, and Fe_5S_2 exhibits Fe surrounded by up to 9 Fe sites with Fe-Fe bond lengths up to 25% shorter in Fe_5S_2 compared to Fe_3S (Table S4). Following previous descriptions of related M_5X_2 phases (e.g. (Kjekshus et al. 1973; Oryshchyn et al. 2011), Fe_5S_2 can be viewed as an arrangement of 6 Fe sites and 3 S sites with the Fe1, Fe2, Fe4, and Fe6 sites in 13-fold

coordination, the Fe3 and Fe5 sites in 12-fold coordination, and the S sites in 10-fold coordination (Figure 2c, Table S4). All sites are coordinated by both Fe and S sites.

The presented single-crystal derived structures of Fe_5S_2, Fe_3S, *C*23 Fe_2S, and *C*37 Fe_2S were then used to interpret the changes in powder X-ray diffraction patterns collected during heating between 110 and 200 GPa and to ~3300 K (Figure 4, Figure S4). *C*23 Fe_2S is observed coexisting with Fe to ~125 GPa and up to ~2300 K. In combination with previous studies, *C*23 Fe_2S is stable at moderate temperatures between 25 and 125 GPa (Zurkowski et al. *in press,* Zurkowski et al. submitted). A pressure-induced *C*23–*C*37 Fe_2S transition is constrained between 125 and 135 GPa, in agreement with previous investigations of Fe_2S (Zurkowski et al. submitted). *C*37 Fe_2S is stable between 130–200 GPa and to ~3000 K in this study, and previous work suggests that *C*37 Fe_2S may remain stable to 306 GPa at high temperatures (Tateno et al. 2019). Tetragonal Fe_3S forms from the reaction of *C*23 Fe_2S + Fe between 2000–2400 K at ~115 GPa. The stability of tetragonal Fe_3S is constrained to pressures below ~120 GPa at high temperatures in Fe-rich systems (Figure 4) (Seagle et al. 2006; Morard et al. 2008; Kamada et al. 2010; Kamada et al. 2012; Thompson et al, 2020). Fe_5S_2 is observed coexisting with iron between ~120–200 GPa and in the 2400–3300 K range, making it the relevant sulfide in the melting and crystallization properties of Fe-rich metallic cores at these pressures (Figure 4).

Sulfur in Earth and planetary cores

The stability of Fe_5S_2 and the phase relations observed in this study present novel constraints on the material properties of Fe-sulfides at conditions relevant to Earth's outer core, Venus' core, and exoplanetary cores of similar size and core-mass fraction (CMF). Namely, at pressures ≥120 GPa, Ni_5As_2-type Fe_5S_2, not tetragonal Fe_3S as previously believed, is the

relevant Fe-rich sulfide. As Earth's outer core crystallizes over time, Fe_5S_2 will eventually crystallize over a large depth range up to the CMB. Tetragonal Fe_3S has been confirmed up to 120 GPa (Figure 4) (Seagle et al. 2006; Morard et al. 2008; Thompson et al., 2020), constraining the $Fe_3S + Fe \rightarrow Fe_5S_2 + Fe$ transition to ~120 GPa. Rocky planetary bodies with sizes and CMFs like that of Venus (CMB = 114 GPa) (Aitta 2012) would likely crystallize Fe_3S at the CMB, while Fe_5S_2 will be crystallizing over much of the core's depth. *C*37 Fe_2S is reported to be stable on the solidus above 306 GPa in Fe-rich systems (Tateno et al. 2019), suggesting a $Fe_5S_2 + Fe \rightarrow Fe_2S + Fe$ transition in the 200–300 GPa range. *C*37 Fe_2S remains the candidate Fe-rich sulfide at Earth's ICB, but for planets like Venus with a central pressure of 274 GPa (Aitta 2012), Fe_5S_2 may instead be the relevant Fe-rich sulfide, necessitating experimental determination of the $Fe_5S_2 \rightarrow Fe_2S + Fe$ decomposition *P-T* boundary. Additional assessment of the volume and melting-temperature changes across these newly determined sulfide transitions are critical for matching the density and seismic profiles of Earth and rocky planetary cores. Furthermore, as Fe_5S_2 exhibits a complex crystalline arrangement with significant metal-metal bonding compared to Fe_2S and Fe_3S at core pressures, the significant depth over which Fe_5S_2 crystallizes in and Venus- to Earth-sized planetary cores is likely to contribute to higher conductivity signatures in these regions.

Terrestrial core chemistries are multicomponent; Si and Ni are also important core-alloying elements in planets such as Earth, drawing attention to the potential stability of the perryite $(Fe, Ni)_8(Si, P)_3$ structure in (Fe, Ni) – (Si, S)-rich cores. Perryite, is a mineral observed in enstatite chondrites and aubrites that adopts a structure that is trigonal stacking variant of the Ni_5As_2-type structure (Wasson and Wai, 1970; Okada et al. 1991) and iron phosphides tend to adopt analogous structures to that observed in iron sulfides (i.e., Fei et al. 2000; Dera et al. 2008;

Gu et al. 2014; Gu et al. 2016; Zurkowski et al., in press). Fe_5S_2 could potentially serve as a host for nickel and silicon in the perryite structure at Earth's outer core conditions. Further, Si has recently been shown to dissolve into iron-sulfide phases and expand their stability fields with pressure (Tao and Fei, 2021). The dissolution of silicon into Fe_5S_2 may expand its stability to higher pressures, making it potentially relevant at Earth's ICB conditions. If this is the case, the partitioning of Si and Ni between $(Fe, Ni)_5(S, Si)_2$ and (Fe, Ni, Si) and the density difference between the inner-core-crystallizing phase and remaining light-element-rich liquid will be crucial to investigations of the inner-core-density deficit and inner core seismic morphology.

Materials and Methods

Experiments targeting multigrain synthesis in the Fe-S system consisted of mixtures of Fe (99.9+%, <10μm, Alfa Aesar) and iron sulfide (FeS, 99.99%, Alfa Aesar) in Fe+12.5 wt% S ($Fe_{80}S_{20}$), Fe + 23 wt% S ($Fe_{67}S_{33}$) compositions. The Fe-FeS compositions were ground in ethanol in a pestle and mortar for 1 hour then mixed dry for a short interval to homogenize any density settling during alcohol evaporation.

Pressure was generated using BX-90-type (Kantor et al. 2012) diamond anvil cells (DAC) with type 1 Boehler-Almax conical diamonds and seats, and Mao symmetric-type DACs with Type 1 standard cut diamonds mounted on tungsten carbide of cubic-boron nitride (cBN) seats. Diamond culets ranged from 150-50 μm in diameter. Foils of $Fe_{80}S_{20}$ or $Fe_{67}S_{33}$ were produced by pressing the Fe–S starting powders between two ungasketed diamond anvils, then loaded between pellets of KCl or SiO_2. Sample chambers ranged from 180-25 μm in diameter and were drilled from pre-indented rhenium gaskets. Samples were dried at 100ºC for 30 minutes prior to pressurization.

Angle dispersive X-ray diffraction (XRD) experiments were conducted at Argonne National Laboratory, sector 13 ID-D, of the Advanced Photon Source. At Sector 13 ID-D, a 2.5 μm x 3.54 μm full width, half maximum (FWHM) monochromatic X-ray beam tuned to 37 or 42 keV was utilized, and diffracted X-rays were collected with a CdTe 1M Pilatus detector. Sample-to-detector geometries were calibrated using a LaB_6 NIST standard and a single crystal of enstatite was used for calibration of the rotational geometry of the X-ray beam and detector.

Double-sided laser heating and *in-situ* XRD collection took place at Sector 13 ID-D. Fibers lasers shaped with ~10 μm radius flat tops were aligned with the X-ray beam using the X-ray fluorescence of the sample pressure media or the gasket (Prakapenka et al., 2008). During heating, thermal emission from a 6 μm central region of the laser-heated spot was measured spectroradiometrically and fit to a gray body approximation (Heinz and Jeanloz, 1987). A 3% temperature correction was then applied to correct for axial gradients through the sample (Campbell et al., 2007; 2009). The laser power on each side of the sample was adjusted to maintain uniform double-sided heating and X-Ray diffraction and temperature measurements were collected every ~200 K with 1s exposure times. Samples were typically quenched at high temperatures within 30-45 minutes of heating or after a phase transition and suitable grain growth was observed. Powder diffraction patterns were processed using Dioptas (Prescher and Prakapenka, 2015) and CrysalisPro (Rigaku OD, 2018). Pressure was determined using the equation of state of hcp-Fe (Dewaele et al. 2006).

Upon quenching, X-ray diffraction maps of the heated spot were collected across a 100 μm^2 square region in 3 μm steps. Map locations showing high intensity, spotty diffraction patterns were chosen for multigrain single-crystal type X-ray diffraction collection approach, as these features indicate high-temperature induced crystallite growth. At chosen map locations, X-

ray diffraction images were collected across ±17 to ±30º rotational scans in 0.25º–0.5º steps with 1– 4 s exposure times. The diffraction reflections were then mapped in the reciprocal space and target grains were identified and separated from reflections associated with the pressure media, iron, and diamond (Rigaku OD, 2018).

Target Fe-S lattices were then indexed and the peak intensities were integrated and reduced using CrysalisPro (Rigaku OD, 2018). Absorption corrections and scaling factors were applied to the structure factors in CrysalisPro using the multi-scan method via the Scale3 Abspack program (Rigaku OD, 2018). The final structure factors and lattice geometries were then refined to known structure models (El-Boragy et al. 1970; Oryshchyn et al. 2011) using SHELXL2014/7 (Sheldrick 2015). Reflections showing anomalous calculated versus measured structure factors; likely due to overlap with diamond and other phases in the multigrain sample, resolution limitations, and volume of crystal illuminated by the X-ray beam, were omitted. Structure models were visualized using Vesta during the refinement procedure (Momma and Izumi 2011).

Acknowledgments

Portions of this work were performed at GeoSoilEnviroCARS (The University of Chicago, Sector 13), Advanced Photon Source (APS), Argonne National Laboratory. GeoSoilEnviroCARS is supported by the National Science Foundation - Earth Sciences (EAR - 1634415). This research used resources of the Advanced Photon Source, a U.S. Department of Energy (DOE) Office of Science User Facility operated for the DOE Office of Science by Argonne National Laboratory under Contract No. DE-AC02-06CH11357. Use of the COMPRES-GSECARS gas loading system was supported by COMPRES under NSF Cooperative Agreement EAR -1606856 and by GSECARS through NSF grant EAR-1634415

and DOE grant DE-FG02-94ER14466. This research used resources of the Advanced Photon Source, a U.S. Department of Energy (DOE) Office of Science User Facility operated for the DOE Office of Science by Argonne National Laboratory under Contract No. DE-AC02-06CH11357.This material is based upon work supported by a National Science Foundation Graduate Research Fellowship to C.C.Z. This work was also supported by the National Science Foundation by grant EAR-1651017 to A.J.C.

Figures

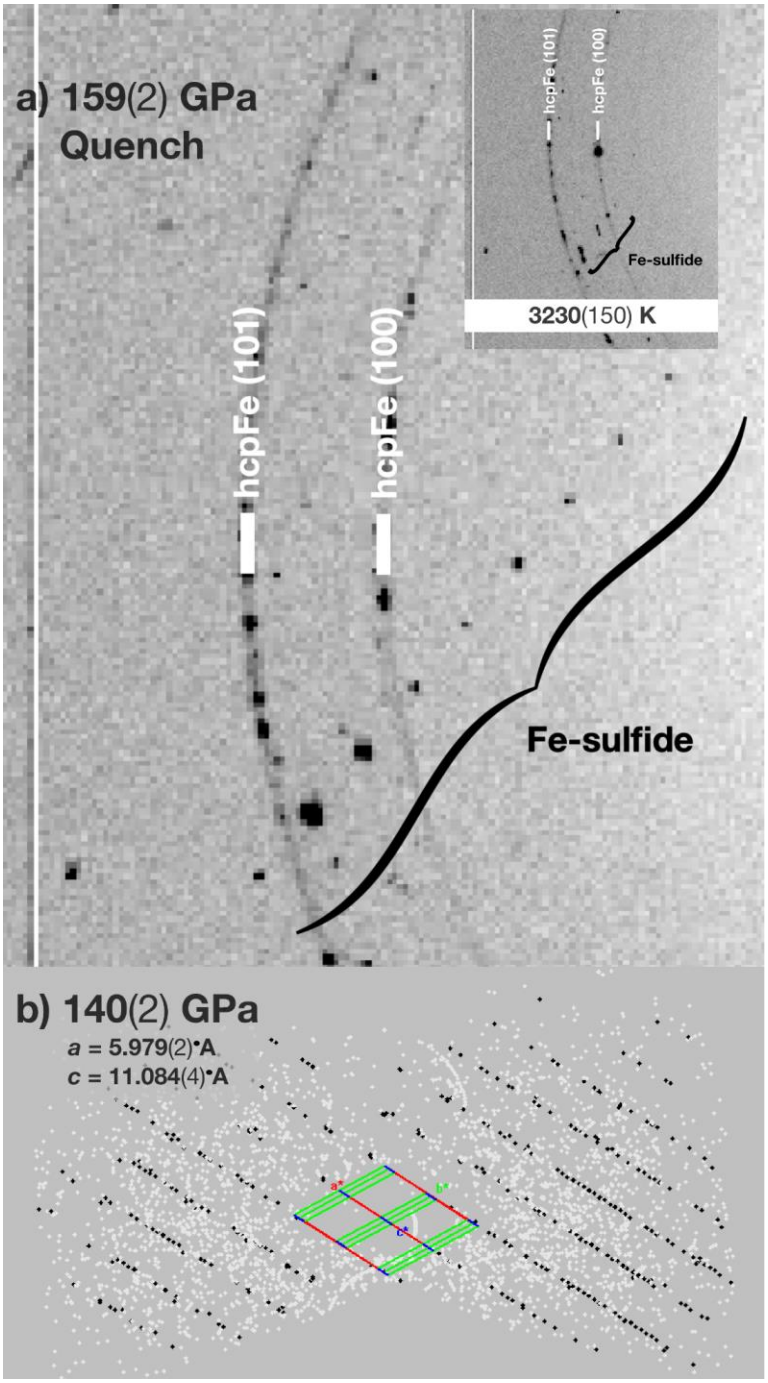

Figure 1. Fe_5S_2 diffraction in equilibrium with iron

a) View of a crystallite of the high-temperature Fe_5S_2 coexisting with recrystallized hcp-Fe after synthesis at 159(2) GPa and 3230(130) K (inset). The spotty rings corresponding to the hcp-Fe (100) and (101) planes demonstrate that iron equilibrated at 159(2) GPa and 3230(130) K. b) View of the reciprocal space for reflections detected in an experiment on the $Fe_{80}S_{20}$ composition quenched from 140(2) GPa and 3070(140) K. The reciprocal lattice, colored in black, is associated with a Fe_5S_2 grain whose lattice parameters are provided in the top left.

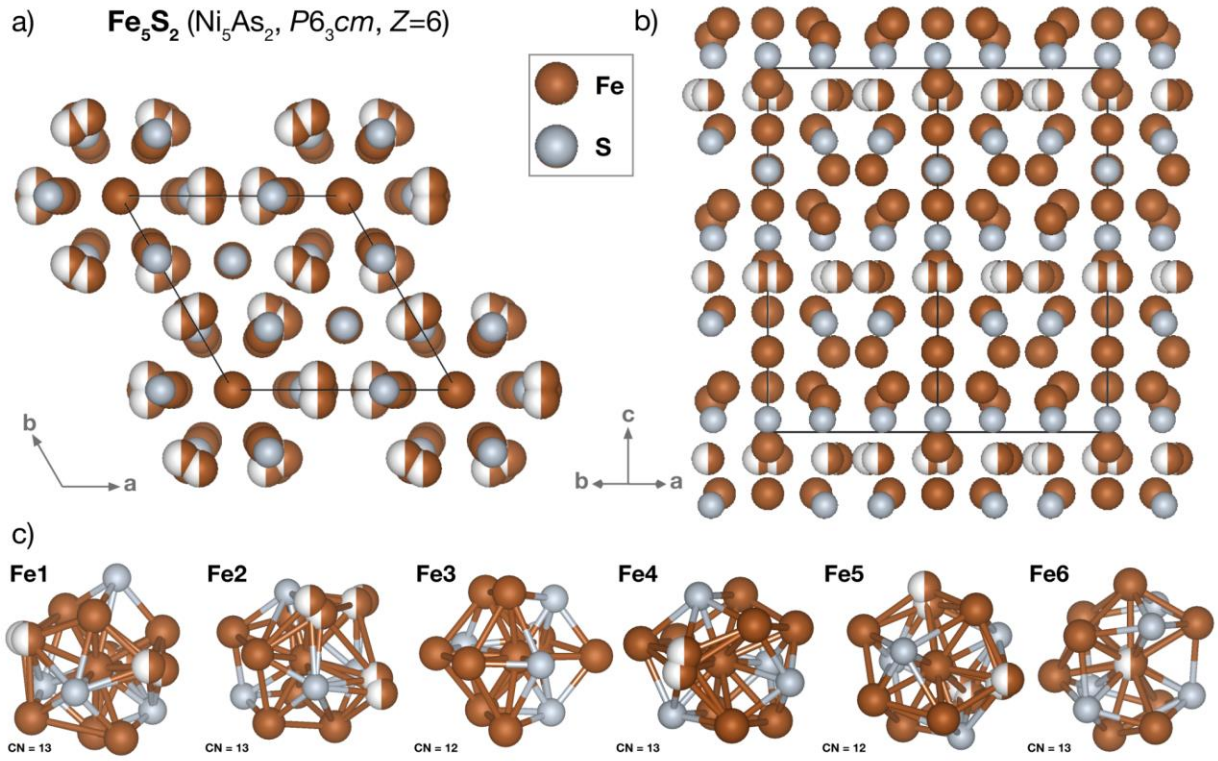

Figure 2. Crystal structure of Ni_5As_2-type Fe_5S_2

Crystal structure of Fe_5S_2 viewed along the a) *c* axis and the b) (100) plane. c) The Fe-coordination polyhedra observed in this atomic arrangement are provided. Fe1, Fe2, Fe4, and Fe6 are coordinated by 13 sites and Fe3 and Fe5 are coordinated by 12 sites. Each coordination polyhedron consists of Fe and S sites.

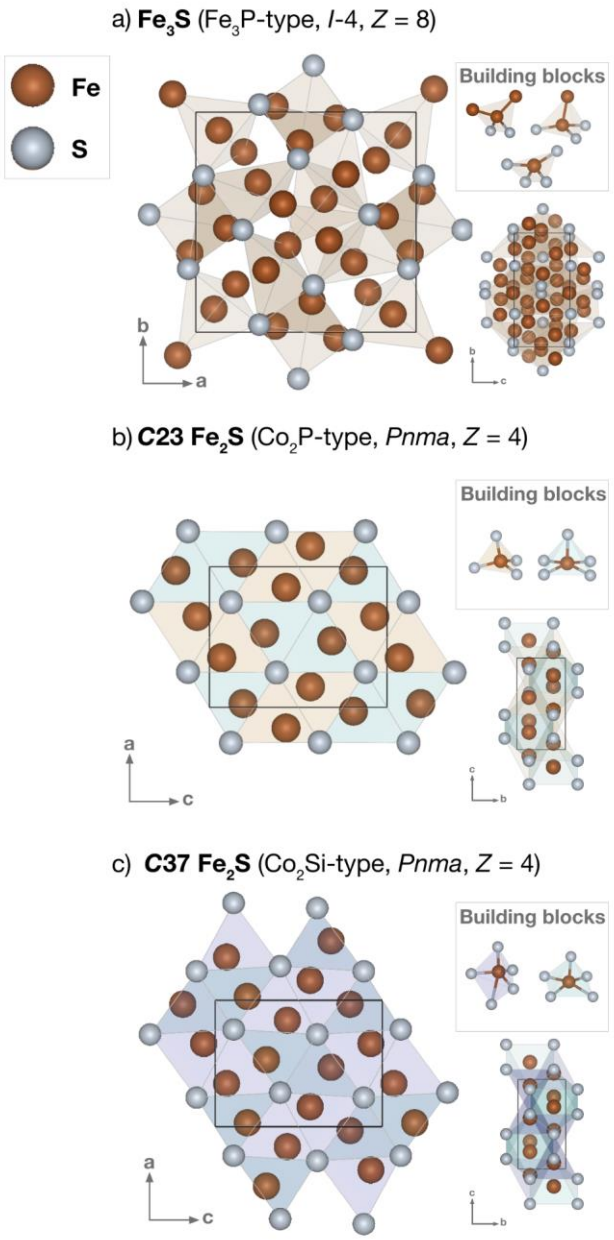

Figure 3. Crystal structures of Fe_3S and Fe_2S observed in this study

a) Fe_3S adopts the Fe_3P-type structure (*I*-4, *Z* = 8) that is composed of three tetrahedrally coordinated Fe-sites, each with increasing Fe–Fe bonding. b) The *C*23 Fe_2S structure (Co_2P-type, *Pnma*, *Z* = 4) is made up of columns of FeS_4 tetrahedra and columns of FeS_5 square pyramids linked along edges in the *b* direction. c) The *C*37 Fe_2S structure (Co_2Si-type, *Pnma*, *Z* = 4) has the same site symmetries as the *C*23 structure, but is marked by a shortened *a* axis and elongated *b* and *c* axes accompanied by the formation of a 5-fold dipyramid.

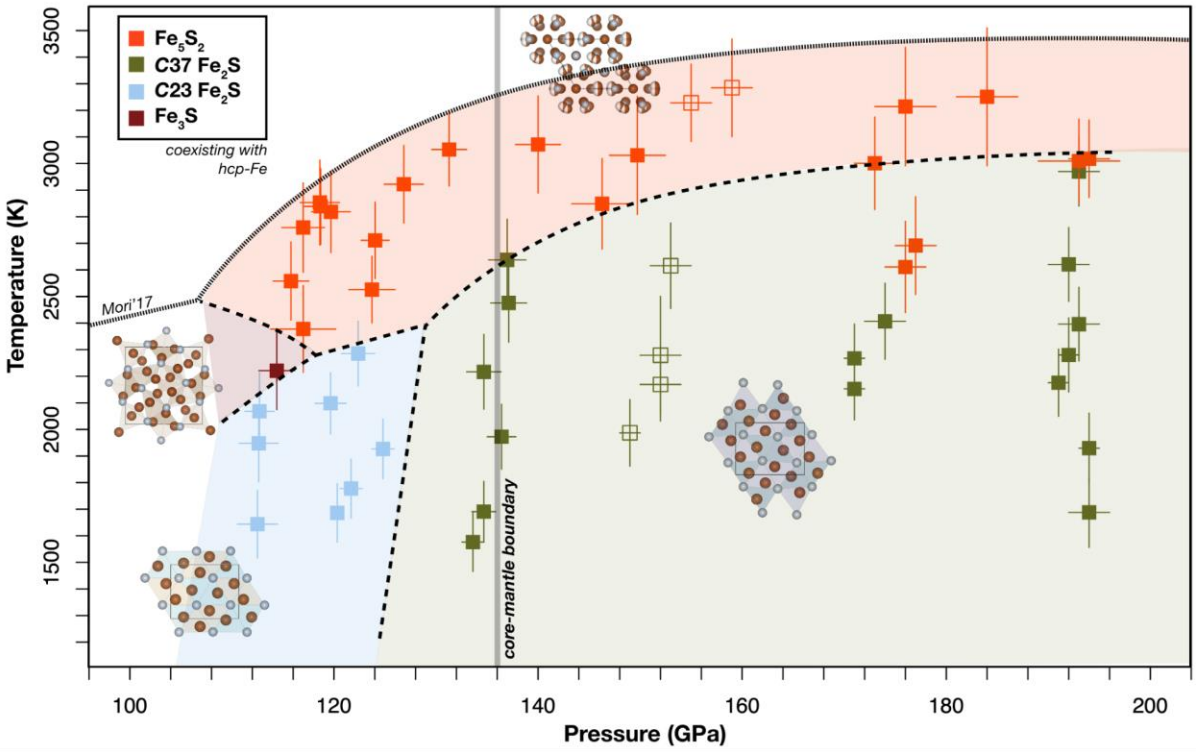

Figure 4. Iron-rich sulfide phase diagram to Earth's outer core pressures

At moderate temperatures up to 130 GPa, *C*23 Fe_2S is observed. At moderate temperatures, tetragonal Fe_3S (Fe_3P-type) is observed below 120 GPa. At moderate temperatures between 130 and 200 GPa, *C*37 Fe_2S is observed, and on the liquidus between ~115–200 GPa, Fe_5S_2 is the liquidus phase. A kink the Fe-S solidus curve (Mori et al. 2017), is presented to account for the change in phase relations and the high temperatures at which Fe_5S_2 was observed. The closed squares represent experiments conducted on the $Fe_{80}S_{20}$ starting material, and the open squares represent experiments conducted on the $Fe_{67}S_{33}$ starting material. Both show compatible results, likely indicating that Fe-rich regions of the $Fe_{67}S_{33}$ foils were probed.

References

Anzellini, S., Dewaele, A., Mezouar, M., Loubeyre, P. and Morard, G. (2013). Melting of iron at Earth's inner core boundary based on fast X-ray diffraction. Science, 340, 464–466.

Birch, F. (1952) Elasticity and constitution of the Earth's interior. Journal of Geophysical Research, 57, 227–286.

Buffett, B.A. (2000) Earth's core and the geodynamo. Science, 288, pp.2007-2012.

Campbell, A.J., Seagle, C.T., Heinz, D. L., Shen, G., and Prakapenka, V.B. (2007) Partial melting in the iron-sulfur system at high pressure: A synchrotron X-ray diffraction study. Physics of the Earth and Planetary Interiors, 162, 119–128.

Campbell, A.J., Danielson, L., Righter, K., Seagle, C.T., Wang, Y. and Prakapenka, V.B. (2009) High pressure effects on the iron–iron oxide and nickel–nickel oxide oxygen fugacity buffers. Earth and Planetary Science Letters, 286, 556–564.

Chen, J.H. and Whitmire, K.H. (2018) A structural survey of the binary transition metal phosphides and arsenides of the d-block elements. Coordination Chemistry Reviews, 355, 271–327.

Dewaele, A., Loubeyre, P., Occelli, F., Mezouar, M., Dorogokupets, P.I. and Torrent, M. (2006) Quasihydrostatic equation of state of iron above 2 Mbar. Physical Review Letters, 97, 215504.

Dziewonski, A.M. and Anderson, D.L. (1981) Preliminary reference Earth model. Physics of the Earth and planetary interiors, 25, 297–356.

El-Boragy, M., Bhan, S. and Schubert, K. (1970) Kristallstruktur von Pd_5Sb_2 und Ni_5As_2 und einigen varianten. Journal of the Less Common Metals, 22, 445–458.

Evans, H.T. (1970) Lunar troilite: crystallography. Science, 167, 621–623.

Fearn, D.R. and Loper, D.E., (1981). Compositional convection and stratification of Earth's core. Nature, 289, 393–394.

Fei, Y., Prewitt, C.T., Mao, H.K. and Bertka, C.M (1995). Structure and density of FeS at high pressure and high temperature and the internal structure of Mars. Science, 268, 1892–1894.

Fei, Y., Bertka, C.M. and Finger, L.W. (1997) High-pressure iron-sulfur compound, Fe_3S_2, and melting relations in the Fe–FeS system. Science, 275, 1621–1623.

Fei, Y., Li, J., Bertka, C.M. and Prewitt, C.T. (2000) Structure type and bulk modulus of Fe_3S, a new iron-sulfur compound. American Mineralogist, 85, 1830–1833.

Fei, Y., Ricolleau, A., Frank, M., Mibe, K., Shen, G. and Prakapenka, V. (2007) Toward an internally consistent pressure scale. Proceedings of the National Academy of Sciences, 104, 9182–9186.

Frank, K. and Schubert, K. (1971) Kristallstruktur von $Ni_{31}Si_{12}$. Acta Crystallographica Section B: Structural Crystallography and Crystal Chemistry, 27, 916–920.

Heinz, D.L., and Jeanloz, R. (1987) Measurement of the melting curve of $Mg_{0.9}Fe_{0.1}SiO_3$ at lower mantle conditions and its geophysical implications. Journal of Geophysical Research, 92, 437–444.

Irving, J.C., Cottaar, S. and Lekić, V. (2018) Seismically determined elastic parameters for Earth's outer core. Science advances, 4, 2538.

Jephcoat, A. and Olson, P., (1987) Is the inner core of the Earth pure iron? Nature, 325, 332–335.

Jones, J.H. and Drake, M.J. (1983). Experimental investigations of trace element fractionation in iron meteorites, II: The influence of sulfur. Geochimica et Cosmochimica Acta, 47, 1199–1209.

Kamada, S., Terasaki, H., Ohtani, E., Sakai, T., Kikegawa, T., Ohishi, Y., Hirao, N., Sata, N. and Kondo, T. (2010) Phase relationships of the Fe–FeS system in conditions up to the Earth's outer core. Earth and Planetary Science Letters, 294, 94–100.

Kamada, S., Ohtani, E., Terasaki, H., Sakai, T., Miyahara, M., Ohishi, Y. and Hirao, N. (2012) Melting relationships in the Fe–Fe_3S system up to the outer core conditions. Earth and Planetary Science Letters, 359, 26–33.

Kantor, I., Prakapenka, V., Kantor, A., Dera, P., Kurnosov, A., Sinogeikin, S., Dubrovinskaia, N. and Dubrovinsky, L. (2012) BX90: A new diamond anvil cell design for X-ray diffraction and optical measurements. Review of Scientific Instruments, 83, 125102.

King, H. and Prewitt, C.T. (1982) High-pressure and high-temperature polymorphism of iron sulfide (FeS). Acta Crystallographica Section B: Structural Crystallography and Crystal Chemistry, 38, 1877–1887.

Kjekshus, A., Skaug, K.E., Hebrew, C., Van Buren, C.T., Klæboe, P. and Swahn, C.G. (1973). On the crystal structure of Ni_5As_2. Acta Chem. Scand., 27, 582–588.

Kruijer, T.S., Touboul, M., Fischer-Gödde, M., Bermingham, K.R., Walker, R.J. and Kleine, T., 2014a. Protracted core formation and rapid accretion of protoplanets. Science, 344, 1150–1154.

Kuwayama, Y., Morard, G., Nakajima, Y., Hirose, K., Baron, A.Q., Kawaguchi, S.I., Tsuchiya, T., Ishikawa, D., Hirao, N. and Ohishi, Y. (2020). Equation of state of liquid iron under extreme conditions. Physical review letters, 124, .165701.

Litasov, K.D., Shatskiy, A.F., Minin, D.A., Kuper, K.E. and Ohfuji, H. (2019). The Ni–Ni_2P phase diagram at 6 GPa with implication to meteorites and super-reduced terrestrial rocks. High Pressure Research, 39, 561–578.

Maaref, S., Madar, R., Chaudouet, P., Fruchart, R., Senateur, J.P., Averbuch-Pouchot, M.T., Bacmann, M., Durif, A. and Wolfers, P. (1983) Etude de la structure et des conditions de stabilite d'un nouvel arseniure de fer: $Fe_{12}As_5$. Materials Research Bulletin, 18, 473-480.

Malvin, D.J., Wang, D. and Wasson, J.T. (1984) Chemical classification of iron meteorites—X. Multielement studies of 43 irons, resolution of group IIIE from IIIAB, and evaluation of Cu as a taxonomic parameter. Geochimica et Cosmochimica Acta, 48, 785–804.

Masters, G. and Gubbins, D. (2003) On the resolution of density within the Earth. Physics of the Earth and Planetary Interiors, 140, 159–167.

McDonough, W.F. and Sun, S.S. (1995) The composition of the Earth. Chemical geology, 120, 223–253.

McDonough, W.F., (2003) 2.15–Compositional model for the earth's core. Treatise on Geochemistry, 547–568.

Momma, K. and Izumi, F. (2011) VESTA 3 for three-dimensional visualization of crystal, volumetric and morphology data. Journal of applied crystallography, 44, 1272–1276.

Morard, G., Andrault, D., Guignot, N., Sanloup, C., Mezouar, M., Petitgirard, S. and Fiquet, G. (2008). In situ determination of Fe–Fe_3S phase diagram and liquid structural properties up to 65 GPa. Earth and Planetary Science Letters, 620–626.

Mori, Y., Ozawa, H., Hirose, K., Sinmyo, R., Tateno, S., Morard, G. and Ohishi, Y. (2017) Melting experiments on Fe–Fe_3S system to 254 GPa. Earth and Planetary Science Letters, 464 135–141.

Murthy, V.R. and Hall, H.T. (1970) The chemical composition of the earth's core: Possibility of sulfur in the core. Physics of the Earth and Planetary Interiors, 2, 276–282.

Nimmo, F. (2015) Thermal and compositional evolution of the core. In Core Dynamics (Ed. Peter Olsen). Vol. 8 Treatise on Geophysics, (Exec. Eds. G. Schubert), 217–241.

Okada, A., Kobayashi, K., Ito, T. and Sakurai, T. (1991) Structure of synthetic perryite, $(Ni, Fe)_8(Si, P)_3$. Acta Crystallographica Section C: Crystal Structure Communications, 47, 1358–1361.

Oryshchyn, S., Babizhetskyy, V., Zhak, O., Stoyko, S., Guérin, R., and Simon, A. (2011) Crystal structure of HT-Ni_5P_2 and reinvestigation of isotypic Ni_5As_2. Intermetallics, 19, 1041–1046.

Ozawa, H., Hirose, K., Suzuki, T., Ohishi, Y. and Hirao, N. (2013) Decomposition of Fe_3S above 250 GPa. Geophysical research letters, 40, 4845–4849.

Prakapenka, V.B., Kubo, A., Kuznetsov, A.Laskin, A., Shkurikhin, O., Dera, P., Rivers, M. L. and Sutton, S.R. (2008) Advanced flat top laser heating system for high pressure research at GSECARS: application to the melting behavior of germanium. High Pressure Research, 28, 225–235.

Prescher, C., and Prakapenka, V.B. (2015) DIOPTAS: a program for reduction of two dimensional X-ray diffraction and data exploration. High Pressure Research, 35(3), 223–230.

Ricard, Y., Šrámek, O. and Dubuffet, F. (2009) A multi-phase model of runaway core–mantle segregation in planetary embryos. Earth and Planetary Science Letters, 284, 144–150.

Rigaku Oxford Diffraction (2018) CrysAlisPRO software system, ver. 1.171.39.44a Rigaku Corporation, Oxford, U.K.

Ringwood, A.E. (1966) The chemical composition and origin of the Earth. Advances in earth science, 65, 287.

Rubie, D.C., Frost, D.J., Mann, U., Asahara, Y., Nimmo, F., Tsuno, K., Kegler, P., Holzheid, A. and Palme, H. (2011) Heterogeneous accretion, composition and core–mantle differentiation of the Earth. Earth and Planetary Science Letters, 301, 31–42.

Rundqvist, S. (1960) The structures of Co_2P, Ru_2P and related phases. Acta Chemica Scandinavica, 14, 1961–1979.

Rundqvist, S. and Jellinek, F. (1959) The structures of Ni_6Si_2B, Fe_2P and some related phases. Acta Chemica Scandinavica, 13, 425–432.

Saini, G.S., Calvert, L.D., and Taylor, J.B. (1964). Compounds of the type M_5X_2: Pd_5As_2, Ni_5Si_2, and Ni_5P_2. Canadian Journal of Chemistry, 42, 1511–1517.

Scott, E.R. and Wasson, J.T. (1975) Classification and properties of iron meteorites. Reviews of Geophysics, 13, 527–546.

Seagle, C.T., Campbell, A.J., Heinz, D.L., Shen, G. and Prakapenka, V.B. (2006) Thermal equation of state of Fe_3S and implications for sulfur in Earth's core. Journal of Geophysical Research: Solid Earth, 111.

Shannon, M.C. and Agee, C.B. (1996) High pressure constraints on percolative core formation. Geophysical Research Letters, 23, 2717–2720.

Sheldrick, G.M. (2015b) Crystal structure refinement with SHELXL. Acta Crystallographica Section C: Structural Chemistry, 71, 3–8.

Stevenson, D.J. (1981). Models of the Earth's core. Science, 214, 611–619.

Stevenson, D.J. (1988) Fluid dynamics of core formation. In Topical Conference Origin of the Earth (Vol. 681, p. 87).

Tateno, S., Ozawa, H., Hirose, K., Suzuki, T., I-Kawaguchi, S., and Hirao, N. (2019) Fe_2S: the most Fe-rich iron sulfide at the Earth's inner core pressures. Geophysical Research Letters, 46, 11,944–11,949.

Thompson, S., Komabayashi, T., Breton, H., Suehiro, S., Glazyrin, K., Pakhomova, A. and Ohishi, Y. (2020) Compression experiments to 126 GPa and 2500 K and thermal equation of state of Fe_3S: Implications for sulphur in the Earth's core. Earth and Planetary Science Letters, 534, 116080.

Wasson, J.T. and Wai, C.M. (1970) Composition of the metal, schreibersite and perryite of enstatite achondrites and the origin of enstatite chondrites and achondrites. Geochimica et Cosmochimica Acta, *34*, 169-184.

Yoshino, T., Walter, M.J. and Katsura, T. (2003) Core formation in planetesimals triggered by permeable flow. Nature, 422, 154–157.

Yokoo, S., Hirose, K., Sinmyo, R. and Tagawa, S. (2019) Melting experiments on liquidus phase relations in the Fe-S-O ternary system under core pressures. Geophysical research letters, 46, 5137–5145.

Zurkowski, C.C., Lavina, B., Chariton, S., Tkachev, S., Prakapenka V.B. and Campbell A.J., *in press*. The crystal structure of Fe_2S at 90 GPa based on single-crystal X-ray diffraction techniques. American Mineralogist, https://doi.org/10.2138/am-2022-7973

Zurkowski, C. C., Lavina, B., Brauser, N. M., Davis, A. H., Chariton, S., Tkachev, S., Greenberg, E., Prakapenka, V. B., and Campbell, A. J., *in press.* Pressure-induced *C*23-*C*37 transition and compression behavior of orthorhombic Fe_2S to Earth's core pressures and high temperatures. https://doi.org/10.2138/am-2022-8187

Fe_5S_2 identified as a host for sulfur in Earth's core

Claire C. Zurkowski[a †], Barbara Lavina[b,c], Abigail Case[a], Kellie Swadba[a], Stella Chariton[b], Vitali B. Prakapenka[b], Andrew J. Campbell[a]

[a]The University of Chicago, Department of the Geophysical Sciences, 5734 S Ellis Ave, Chicago, IL 60637, USA
[b]Center for Advanced Radiation Sources, The University of Chicago, 9700 South Cass Avenue, Lemont, IL 60439, USA
[c]X-ray Science Division, Advanced Photon Source, Argonne National Laboratory, Lemont, IL 60439, USA
[†]Now at Earth and Planets Laboratory, Carnegie Institution for Science, 5251 Broad Branch Road, NW, Washington, DC 20015, USA

Corresponding Author: Claire Zurkowski, czurkowski@carnegiescience.edu

Supplementary Information

The Supplementary Information includes:

- Supplementary Information Text
- Table S1
- Table S2
- Table S3
- Table S4
- Figure S1
- Figure S2
- Figure S3
- Figure S4
- Supplementary Information References

Supplementary Information Text

Synthesis of Fe_5S_2 to 200 GPa

Fe_5S_2 was synthesized between 119(2) and 193(4) GPa with heating to temperatures between 2400–3300 K. The formation of Fe_5S_2 phase was first recognized in the diffraction patterns by the onset of diffuse streaks and sets of closely spaced reciprocal nodes in the powder diffraction images, suggesting a complex atomic arrangement (Figure 1, S1). With sustained high temperatures in the samples loaded in more hydrostatic pressure media (e.g. KCl vs. SiO_2), large grain growth (3 – 6 μm) was observed and the diffuse streaks became less apparent. Further experiments are required to assess the role of hydrostaticity, kinetics, pressure, and temperature on the disorder of this phase.

Recrystallization of hcp-Fe with the Fe_5S_2 crystallites at high temperatures was observed in all experiments using the $Fe_{80}S_{20}$ and $Fe_{67}S_{33}$ starting powders as evidenced by the spotty (100) and (101) hcp-Fe rings in Figure 1a. Fe-recrystallization with this high-temperature Fe-sulfide establishes that the probed sample locations were in a Fe-saturated phase-field (Figure 1a) and this phase is important to consider further in the context of Fe-rich planetary cores.

Upon temperature quenching, rotational single-crystal X-ray diffraction scans were performed across a 37–60º omega range, depending on the DAC configuration, and grains were indexed in the reciprocal space to a hexagonal unit cell compatible with an Fe_5S_2 volume (Table S1, Figure 1b). Three unit-cell polytypes were observed and indexed in our experiments and are listed in Table S1. All indexed grains exhibit an *a* axial length of ~ 6 Å, while 3 differing *c* axial lengths are observed: ~ 11, 26, and 73 Å. Diffraction mappings show that the polytypism is accompanied by diffuse scattering suggesting positional disorder as the atomic arrangement along the *c* axis configures at high temperatures (Figure S1). Analogous polytypism has also

been observed in the transition metal binary phase Pb_5As_2 (Saini et al. 1964). Decreased diffuse scattering from the Fe_5S_2 grains was observed after continued heating in the KCl pressure media, and grains with $a \sim 6$ Å, $c \sim 11$ Å were indexed, indicating that this configuration is the most positionally ordered arrangement relevant to these high *P-T* conditions. These measured unit cell parameters are compatible with 6 formula units per cell volume of Fe_5S_2.

The structure of a grain Fe_5S_2 synthesized at 140(2) GPa and 3070(180) K was determined based on 159 observed reflections at these extreme conditions (Table S2). Assessment of the systematic absences for the structure factors reduced for Fe_5S_2 suggests a $P6_3cm$ space group. Structural solution and positional and displacement parameter refinement converged on the Ni_5As_2 structure type (Table S2, 3; Figure 2) (Oryshchyn et al. 2011). The Ni_5As_2 structure is a slight modification of the Pb_5Sb_2 structure (El-Boragy et al. 1970) where the Fe6 site (Table S3) is split about its position and given half occupancy, changing its Wyckoff site from 6c to 12d (Figure 2) (Oryshchyn et al. 2011). This structural modification was initiated based on the large U_{22} parameter observed on the *M*6 site (*M* = metal) in Ni_5As_2 when anisotropic displacement parameters were refined using a Pb_5As_2 starting model (Figure S2). In the current dataset, a comparably large U_{22} value was observed on the Fe6 site resulting in an oblong displacement ellipse when refining the data against the initial Pb_5As_2 structure model. The Fe6 site was positionally disordered following Oryshchyn et al. (2011), and the resultant R_1 value was improved by around ~5%, rendering the Ni_5As_2 structure model more compatible with the current Fe_5S_2 data (Table S2). Isotropic displacement parameters showing errors > 3**σ** were fixed to a value equal to approximately the average displacement parameter value for Fe or S (Table S2). The isotropic displacement parameter for the disordered Fe site was also fixed at an average Fe_{Uiso} value (Table S2). The number of reflections collected at these extreme pressures

limits the number of statistically meaningful parameters to refine, and fixing displacement parameters to reasonable values precludes overinterpretation of the current dataset. The high isotropic displacement parameter observed on the Fe4 site may represent some vacancies on this site, but the dataset is again deficient to precisely describe the site occupancy.

The experimental details for the solution and refinement of Fe_5S_2 to the Ni_5As_2 solution model are provided in Table S2 and the atomic coordinates of Fe_5S_2 synthesized at 140(2) GPa and 3070(180) K are provided in Table S3. In accordance with previous descriptions of related M_5X_2 transitional-metal binary phases (e.g. (Kjekshus et al. 1973; Oryshchyn et al. 2011), Fe_5S_2 can be viewed as an arrangement of 6 Fe sites and 3 S sites with the Fe1, Fe2, Fe4, and Fe6 sites are in 13-fold coordination, the Fe3 and Fe5 sites are in 12-fold coordination, and the S sites are in 10-fold coordination (Figure 2c). The measured bond lengths for the Fe-coordinated polyhedra are provided in Table S4. All sites are coordinated by both Fe and S sites. A CIF file for Fe_5S_2 is provided in Appendix A1.

Final R_1 values $\simeq$ 10% attest to the less-than ideal quality of the multigrain dataset as a possible result of the 1-2 megabar synthesis conditions and observed *c* axial disorder and stacking complexities in Fe_5S_2 (Table S2). Previous studies of isomorphic Ni_5As_2 and related Pb_5As_2 at ambient conditions have also reported similar quality of refinements despite obtaining significantly more reflections in the absence of a DAC (e.g. Saini et al. 1964; El-Boragy et al. 1970; Kjekshus et al. 1973). Notable challenges regarding the refinement of the Fe_5S_2 structure model at these extreme conditions are discussed here and compared with similar difficulties reported in previous characterizations of this structure.

Thirteen violations of the $P6_3cm$ systematic absence condition: l = 2n for (0kl), were flagged during the refinement of Fe_5S_2. The reflections associated with these systematic absence

violations were examined in the raw diffraction images and all show low, diffuse intensity. Discrepancy over the presence or absence of weak reflections with (0*kl*), *l*=2n+1 has been reported in previous investigations of Ni_5As_2 and Pb_5As_2 (e.g. Saini et al. 1964; El-Boragy et al. 1970; Kjekshus et al. 1973), suggesting that these studies may have also faced difficulties with space group determination. Observations of these low-intensity reflections may be a result of residual disorder in the stacking arrangement along the *c* direction, and longer heating cycles may be required for the atoms to arrange into equilibrium positions. It is likewise possible that varying synthesis methods for Ni_5As_2 and Pb_5As_2 in previous ambient condition studies affected the *c* axial atomic arrangement. Ni_5As_2 and isomorphic Ni_5P_2 also exhibits a homogeneity range of ~71.25 – 72.7 atomic % As (Kjekshus et al. 1973; Litasov et al., 2019), and slight modifications of this structure based on varying stacking arrangements result in structures such as $Ni_{31}Si_{12}$ (Frank and Schubert 1971) and $(Fe, Ni)_8(Si, P)_3$ (perryite) (Okada et al. 1991). Attempts to refine the current Fe-sulfide phase with the $Ni_{31}Si_{12}$ or perryite structure models did not improve the refinement results. Based on the presence of disorder, polytypism, anisotropic vibrational motion, and nonstoichiometry in the related M_5X_2 phases, additional nuances to the Fe_5S_2 structure model may be developed in future studies; however, the identification and characterization of the Fe_5S_2 crystal structure determined here to 200 GPa is novel, and the observations and challenges reported in this study align with that of previous analyses of Ni_5As_2 and Pb_5Sb_2 that were not limited by microdiffraction in a DAC at extreme conditions.

Other sulfides observed during heating to 200 GPa

Three experiments and 7 heating cycles were performed in this study between 100 and 200 GPa and to 3400 K, and the X-ray diffraction patterns collected upon heating provide insight

602 into the Fe-rich Fe-S phase relations at outer core pressures and to high temperatures. In each
603 heating experiment, near melting temperatures were targeted and grains of Fe_5S_2 were identified
604 upon quenching. Additional Fe-sulfides were also observed across the thermal gradient of the
605 heated spot, providing information on the lower temperature Fe-saturated phase relations in each
606 heating cycle. Upon quenching from high-temperature synthesis at 119(2) GPa, the other grains
607 in the sample were identified and indexed to a tetragonal cell with a = 8.094(3) Å, c = 3.990(2)
608 Å, compatible with 8 formula units of Fe_3S (Table S1). The structure was then solved and refined
609 to the Fe_3P-type structure (I-4, Z = 8) (referred to herein as I-4 Fe_3S) in agreement with previous
610 studies (Fei et al. 2000; Seagle et al. 2006; Morard et al. 2007; Kamada et al. 2010; Kamada et
611 al. 2012; Thompson et al. 2020). The resultant structure model for Fe_3S at these conditions is
612 shown in Figure (3a), a CIF file for Fe_3S is provided in Appendix A2, and the refinement details
613 are given in Table S2. The structure can be viewed as containing 3 tetrahedrally coordinated Fe
614 sites (Blanchard et al. 2008): one Fe-site is coordinated only by S atoms with an average bond
615 length of 2.083(9) Å, another Fe site is coordinated by 3 S atoms and 1 Fe atom with an average
616 bond length of 2.146(8) Å, and the third Fe site is coordinated by 2 S and 2 Fe atoms with an
617 average bond length of 2.137(8) Å (Figure 3). The measured interatomic distances are
618 comparable to reports on other transition metal M_3X structures (e.g. Aronnson 1955; Rundqvist
619 1979).

620 After temperature quenching from 131(2) GPa and 3050(140) K, grains of Fe_3S were not
621 observed across the heated spot. Instead, orthorhombic lattices were also identified with
622 parameters a = 4.869(2) Å, b = 3.256(2) Å, c = 6.139(2) Å, compatible with 4 formula units of
623 Fe_2S. Structural solution and refinement indicate that the Fe_2S grains adopt the C23 structure
624 (Co_2P type, *Pnma*, Z = 4) in agreement with previous structural analyses at lower pressures

(Zurkowski et al. in press). Refinement details for the structure model are given in Table S2 and a CIF file for *C*23 Fe_2S is provided in Appendix A3. The structure is composed of columns of FeS_4 tetrahedra and columns of FeS_5 square pyramids linked along edges in the *b* direction (Figure 3b). The average Fe–S bond lengths are 2.213(8) Å and 2.011(2) Å in the square pyramids and tetrahedra, respectively. These values are comparable with that observed in *C*23 Fe_2S at 90 GPa (Zurkowski et al. *in press*).

Upon compression and heating at 140(2) GPa and 3070(180) K, orthorhombic grains were identified in the sample chamber with a = 4.667(2) Å, 3.289(1) Å, 6.186(4) Å. This unit cell is similar to the *C*23 Fe_2S observed at 130 GPa, but exhibits a 4 % contraction of the *a* axial length, a 1% extension of the *b* and *c* axial lengths, and a 2% volume decrease. Structural solution and refinement using the measured structure factors establish that Fe_2S adopts the *C*37 structure (Co_2Si-type, *Pnma, Z*=4) at these conditions (Figure 3c). A CIF file for *C*37 Fe_2S is provided in Appendix A4 and the analysis details are given in Table S2. In agreement with the proposed *C*23–*C*37 Fe_2S phase transition around 140 GPa that is accompanied 1.6% volume decrease (Zurkowski et al., *in press*), this work confirms that the *C*23–*C*37 transition in Fe_2S occurs between 130 and 140 GPa with a similar volume change. Inherent to the *C*23–*C*37 transition is coordination change from the 4-fold Fe1 coordination polyhedra in the *C*23 structure to the 5-fold dipyramid polyhedra in the *C*37 structure (Figure 3b, c). Comparing the *C*23 and *C*37 structure models determined at 130 and 140 GPa, respectively, a 10% contraction of the interatomic distance involved in the coordination change is observed (Figure S3). The average Fe–S bond lengths measured in *C*37 Fe_2S are 2.196(2) Å and 2.165(3) Å in the square pyramids and dipyramids, respectively. These values are comparable with *C*23 Fe_2S.

Fe-rich sulfide phase relations at core-mantle boundary pressures

The presented single-crystal derived structures of Fe_5S_2, Fe_3S, *C*23 Fe_2S and *C*37 Fe_2S were then used to inform the changes in diffraction patterns collected during heating between 110 and 200 GPa and to ~3300 K. Beginning at 112 GPa, diffraction signal from *C*23 Fe_2S coexisting with Fe was first identified upon heating of the $Fe_{80}S_{20}$ starting material to ~2000 K. With continued heating, peaks associated with tetragonal Fe_3S were observed over a limited temperature range ($\lesssim$ 2400 K) until diffuse scattering signal and Bragg reflections from Fe_5S_2 first appeared. Crystallization of the Fe_5S_2 grains with iron occurred with continued heating to 119(2) GPa and 2840(180) K. Upon heating beginning at 120 GPa, *C*23 Fe_2S was observed coexisting with Fe to 122(1) GPa and 2290(120) K, above which the onset of diffraction from the Fe_5S_2 phase was identified and Fe_5S_2 crystallites formed coexisting with hcp-Fe to 131(2) GPa and 3050(140) K. *I*-4 Fe_3S was not observed. With continued heating cycles between 133(1) GPa and 194(2) GPa and up to 3300 K, *C*37 Fe_2S coexists with Fe at moderate temperatures and a phase transition to Fe_5S_2 occurs at high temperatures. A phase diagram satisfying these observations is proposed in Figure 4, and integrated XRD patterns for the heating cycles at 119(2) and 184(3) GPa and to 3300 K are shown in Figure S4 to demonstrate the identification of *C*23 Fe_2S, Fe_3S, *C*37 Fe_2S, and Fe_5S_2 coexisting with hcp-Fe. The peak intensities from the Fe_5S_2 lattices vary during heating up at high temperatures as a result of disorder, polytypism, and the formation of large crystallites at high temperatures (Figure 1, S1). These structural complexities render the powder diffraction patterns difficult to characterize without incorporating single-crystal XRD techniques.

Discrepancies among the current and previous studies

Transitional metal binary compounds with metal-to-nonmetal ratios ranging from 2.33–2.66 (~70–73 atm% metal) predominantly adopt complex trigonal or hexagonal structures with considerable metal-metal bonding (Chen and Whitmire 2018 and references therein). Our observations of the disorder, polytypism, and complex coordination environments inherent to Fe_5S_2 demonstrate that it aligns with this systematic characterization. Interestingly, the Fe_5S_2 atomic arrangement is thermodynamically favored at the extreme conditions of Earth's outer core over that of *I*-4 Fe_3S. These results are contrary to previous reports of Fe_3S stability on to high temperatures in Fe-rich systems to 250 GPa (Kamada et al. 2010; Kamada et al. 2012; Ozawa et al. 2013; Mori et al. 2017). Few lines of reasoning may account for these discrepancies. Interpretation of Fe_5S_2 in the integrated powder diffraction patterns is difficult due to the variation in diffraction signal obtained from the Fe_5S_2 polytypes and the low intensity scattering from the disordered sites during its formation. Fe_5S_2 also forms large crystallites, limiting the orientations of the phase and rendering indexation of all diffraction angles for Fe_5S_2 quite challenging without rotating the sample. The implementation of single-crystal X-ray diffraction techniques at high pressures was critical in the current study to accurately characterize the hexagonal unit cell geometry and complex structure of the Ni_5As_2-like Fe_5S_2.

Several studies have also reported chemically analyzed Fe_3S grains in samples recovered from high temperatures in the 200–250 GPa range (Mori et al. 2017; Yokoo et al. 2019; Ozawa et al. 2013), but the difference in Fe content between Fe_3S and Fe_5S_2 may be as few as 3%. This value is generally within 3 sigma of the atomic percent error reported for chemical analyses of samples recovered from these extreme conditions, posing another challenge for distinguishing between the synthesis of Fe_3S and Fe_5S_2. Furthermore, based on characterizations of the

693 isomorphic Ni_5As_2 and Ni_5P_2, these structures exhibit a homogeneity range with up to ~73 atm%
694 metal (Kjekshus et al. 1973; Litasov et al., 2019). For example, TEM analysis of a Fe–S sample
695 recovered from 236 GPa and 2980 K reveals sulfide grains with on average ~73 atm% Fe
696 (Ozawa et al. 2013). This value is within 0.3–1.25 atomic percent of the possible range of Fe_5S_2
697 stoichiometries and 2 atomic percent less than an Fe_3S composition. The results from this
698 previous work as well as other chemical analyses of samples recovered from outer core pressures
699 and high temperatures therefore do not contradict the current results (Mori et al. 2017; Yokoo et
700 al. 2019; Ozawa et al. 2013) and may reveal a previous misinterpretation of Fe_5S_2 as Fe_3S based
701 on measured chemistries.
702
703

Table S1. Unit cell parameters of Fe_5S_2, Fe_3S, and Fe_2S measured upon quenching from high *P-T* synthesis in this study. Each cell was indexed in the reciprocal space, and the DAC opening, and number of reflections obtained for each lattice are listed. For select experiments, high-temperature synthesis was conducted without collecting X-ray diffraction data, and the synthesis conditions for these experiments are listed as "high T, not measured."

			Room temperature collection							Synthesis conditions	
	Starting		Phase	P	*a*	*b*	*c*	V	DAC opening	no. of reflections	*P*	*T*
Sample name	material	medium		GPa	Å	Å	Å	Å^3	(°)		GPa	K
C140_P2_map25	Fe80S20	KCl	Fe5S2	105(2)	6.020(4)		11.204(7)	351.6(5)	60	290	119(2)	2840(140)
C140_P2_map31	Fe80S20	KCl	Fe5S2	105(2)	6.050(2)		73.0(2)	2313(1)	60	134	119(2)	2840(140)
C140_P4_map10	Fe80S20	KCl	Fe5S2	118(1)	5.983(3)		11.078(6)	343.4(4)	60	489	140(2)	3070(180)
C140_P4_map14	Fe80S20	KCl	Fe5S2	118(1)	5.979(2)		11.084(4)	343.2(3)	60	379	140(2)	3070(180)
C140_P4_map14	Fe80S20	KCl	Fe5S2	118(1)	5.973(1)		11.094(2)	342.8(1)	60	276	140(2)	3070(180)
C129_P140_map71	Fe67S33	SiO2	Fe5S2	136.4(5)	5.957(4)		71.89(4)	2209(3)	34	84	159(2)	3230(150)
C129_P150_map9	Fe67S33	SiO2	Fe5S2	144.2(8)	5.939(3)		25.99(6)	794(2)	34	76	high T, not measured	
C129_P150_map9	Fe67S33	SiO2	Fe5S2	144.2(8)	5.923(1)		26.004(6)	789.9(3)	34	146	high T, not measured	
C137_P1_map25	Fe80S20	SiO2	Fe5S2	159(1)	5.890(3)		25.837(7)	776.2(5)	40	108	184(3)	3250(260)
C137_P1_map25	Fe80S20	SiO2	Fe5S2	159(1)	5.880(1)		25.789(3)	772.0(2)	40	108	184(3)	3250(260)
C137_P1_map25	Fe80S20	SiO2	Fe5S2	159(1)	5.876(2)		25.884(8)	774.0(4)	40	116	184(3)	3250(260)
C137_P1_map25	Fe80S20	SiO2	Fe5S2	159(1)	5.883(3)		25.85(1)	774.6(7)	40	126	184(3)	3250(260)
C137_P1	Fe80S20	SiO2	Fe5S2	159(1)	5.897(3)		25.90(1)	775.1(6)	40	116	184(3)	3250(260)
C137_P1	Fe80S20	SiO2	Fe5S2	159(1)	5.878(1)		25.784(3)	771.6(2)	40	149	184(3)	3250(260)
C137_P2_34	Fe80S20	SiO2	Fe5S2	179(1)	5.8400(7)		25.583(2)	755.7(1)	40	189	193(4)	3010(160)
C140_P1_map	Fe80S20	KCl	Fe3S	100(1)	8.156(3)		4.025(3)	267.8(3)	60	416	high T, not measured	
C140_P2_map25	Fe80S20	KCl	Fe3S	105(2)	8.094(3)		3.990(2)	261.4(2)	60	296	119(2)	2840(140)
C140_P3_map6	Fe80S20	KCl	*C*23Fe2S	111(1)	4.869(2)	3.256(2)	6.139(2)	97.3(1)	60	227	131(2)	3050(140)
C140_P4_map10	Fe80S20	KCl	*C*37 Fe2S	118(1)	4.677(2)	3.289(1)	6.186(4)	95.18(9)	60	188	140(2)	3070(180)

Table S2. Select experimental details for crystal structure synthesis and analysis of Fe_5S_2, Fe_3S, and the Fe_2S polymorphs.

Phase	**Fe_5S_2**	**Fe_3S**	***C*23 Fe_2S**	***C*37 Fe_2S**
Sample Name	**C140_P4_map10**	**C140_P2_map25**	**C140_P3_map6**	**C140_P4_map10**
Synthesis				
Pressure (GPa)	140(2)	119(2)	131(2)	140(2)
Synthesis Temperature (K)	3070(180)	2840(140)	2050(140)	3070(180)
Symmetry	Hexagonal, *P*6(3)*cm*, Z=6	Tetragonal, *I*-4, Z=8	Orthorhombic, *Pnma*, *Z* = 4	Orthorhombic, *Pnma*, *Z* = 4
a (Å)	5.979(2)	8.094(3)	4.869(3)	4.677(2)
b (Å)			3.256(4)	3.289(1)
c (Å)	11.087(6)	3.990(2)	6.139(2)	6.186(4)
V (Å^3)	343.2(3)	226.4(2)	97.3(1)	95.18(9)
Reduction				
No. of measured, independent and observed [I > 2σ(I)] reflections	396, 309, 157	332, 314, 219	227, 208, 112	188, 158, 105
R_{int}, R_{sigma}	0.092, 0.062	0.053, 0.072	0.012, 0.016	0.009, 0.014
Refinement				
$R[F^2 > 2\sigma(F^2)]$, $wR(F^2)$, S	0.098, 0.255, 1.12	0.067, 0.164, 1.05	0.053, 0.149, 1.21	0.047, 0.139, 1.22
No. of reflections	156	219	112	105
No. of parameters	21	17	10	10
$\Delta\rho_{max}$, $\Delta\rho_{min}$ (e Å^{-3})	2.14, -2.18	1.92, -1.68	1.86, -2.02	1.91, -2.21

Table S3. Atomic coordinates of the Fe_5S_2 refinement model for the data collected at 140(2) GPa and quenched from 3070(180) K.

Wycoff site	ATOM	x	y	z	Uiso
2a	**Fe1**	0	0	0.963	0.021
	error			0.003	0.005
4b	**Fe2**	1/3	2/3	0.089	0.046
	error			0.003	0.005
6c	**Fe3**	0.259	0	0.126	0.021
	error	0.002		0.001	
6c	**Fe4**	0.613	0	0.222	0.021
	error	0.002		0.001	0.003
6c	**Fe5**	0.284	0	0.330	0.027
	error	0.002		0.001	0.003
12d	**Fe6***	0.651	0.056	0.426	0.021
	error	0.003	0.003	0.002	
2a	**S1**	0	0	0.220	0.026
	error			0.004	
4b	**S2**	1/3	2/3	0.299	0.026
	error			0.002	
6c	**S3**	0.673	0	0.030	0.026
	error	0.005		0.003	

*indicates half occupancy

Table S4. Selected interatomic distances for the Fe sites measured in Fe_5S_2 at 140 GPa.

Atom	bonded to	#	distance (Å)
Fe1	–Fe3	3	2.39(2)
	–Fe5	3	2.22(3)
	–Fe6	3	2.313(17)
	–S1	1	2.66(8)
	–S4	3	2.09(3)
Fe2	–Fe3	3	2.275(3)
	–Fe4	3	2.375(16)
	–Fe6	3	2.40(3)
	–S3	1	2.36(4)
	–S4	3	2.108(13)
Fe3	–Fe1	1	2.39(2)
	–Fe2	2	2.275(8)
	–Fe4	3	2.350(15)
	–Fe5	1	2.30(3)
	–Fe6	1	2.307(17)
	–S1	1	1.90(4)
	–S4	3	2.68(3)
Fe4	–Fe2	2	2.375(16)
	–Fe3	3	2.320(11)
	–Fe5	3	2.416(14)
	–Fe6	1	2.303(17)
	–S1	1	2.326(11)
	–S3	2	2.044(16)
	–S4	1	2.10(3)
Fe5	–Fe1	1	2.22(3)
	–Fe3	1	2.30(3)
	–Fe4	3	2.416(14)
	–Fe6	3	2.135(15)
	–S1	1	2.09(5)
	–S3	2	2.184(10)
	–S4	1	2.27(3)
Fe6	–Fe1	1	2.313(17)
	–Fe2	2	2.40(3)
	–Fe3	1	2.307(17)
	–Fe4	1	2.303(17)
	–Fe5	3	2.135(15)
	–S3	2	2.15(3)
	–S4	3	2.17(3)

Figure S1. Unwarped diffraction mappings of the (1*kl*), (0*kl*), and (-1*kl*) directions for an Fe_5S_2 crystallite exemplifying the diffuse scattering signal collected at 119(2) and 2840(180) K. The (1*kl*) and (-1*kl*) mappings also show the presence of a polytype with more closely spaced reflections oriented ~51º from the mapped crystallite.

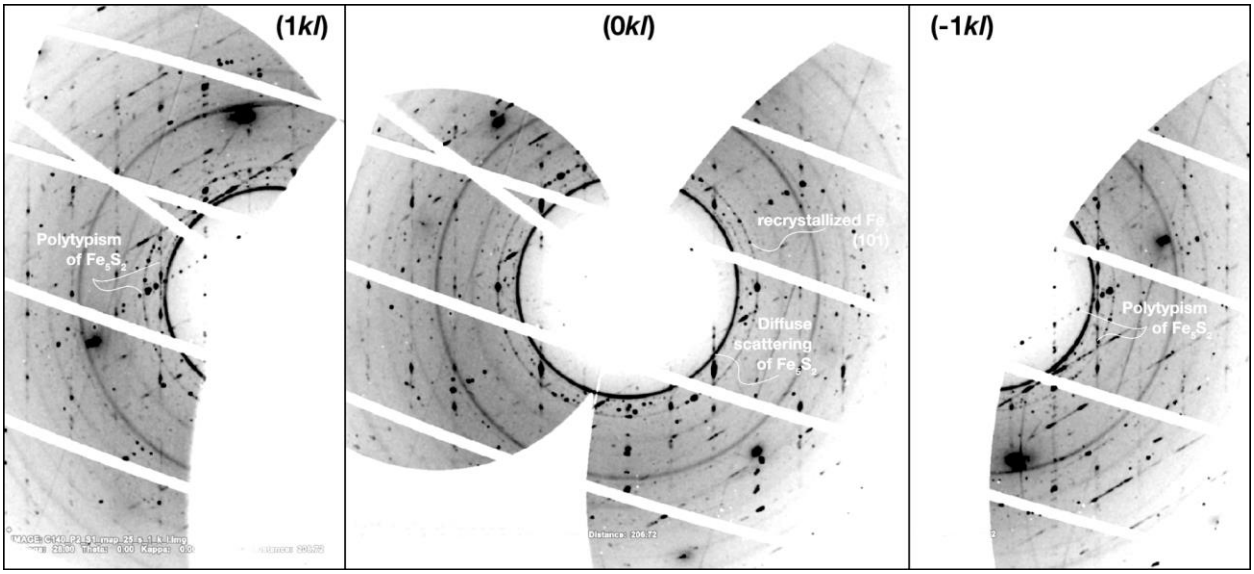

Figure S2. Fe_5As_2 structure model shown with anisotropic displacement ellipsoids using the starting Pb_5As_2 structure model. In accordance with the Ni_5As_2 structural characterization (Oryshchyn et al. 2011), these sites were disordered about their position and ascribed half occupancy.

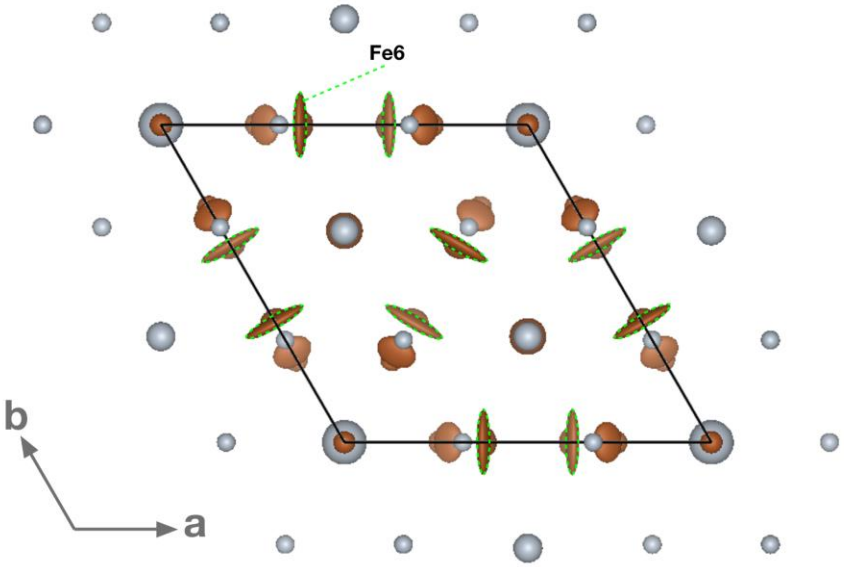

Figure S3. Comparison of the *C*23 and *C*37 structure models refined at 130 and 140 GPa, respectively. In the *C*23 Fe_2S structure, the next nearest sulfur site to the Fe1 tetrahedral site is at a 2.963(1) Å distance at 130 GPa (dotted line). A 10% contraction of this interatomic distance and a coordination change is observed in the formation of *C*37 Fe_2S at 140 GPa (right).

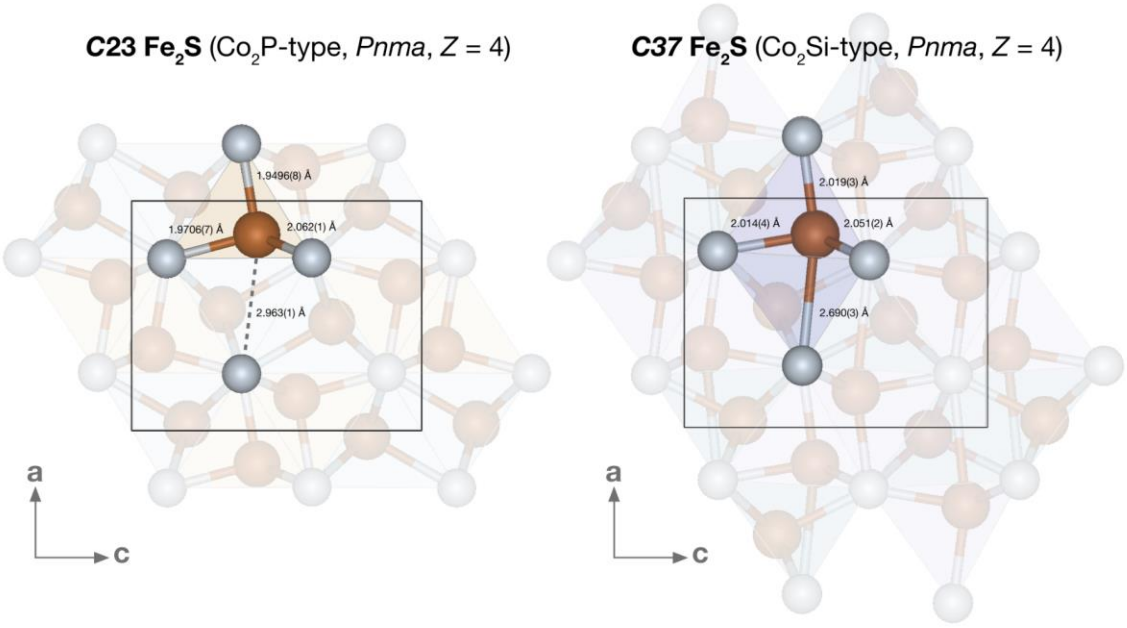

Figure S4. X-ray diffraction patterns collected upon heating in an $Fe_{80}S_{20}$ starting composition at a) 119(2) GPa and b)184(3) GPa. The miller indices for *C*23 Fe_2S (blue), Fe_3S (burgundy), and *C*37 Fe_2S (green) are provided, and the red "H" symbols represent the observations of the formation of Fe_5S_2. The growth of large crystallites, along with the disorder and polytypism of this phase make for challenging powder diffraction indexing, but the lattice parameters of Fe_5S_2 indexed in the reciprocal space after quenching from these high *P*-*T* conditions are provided.

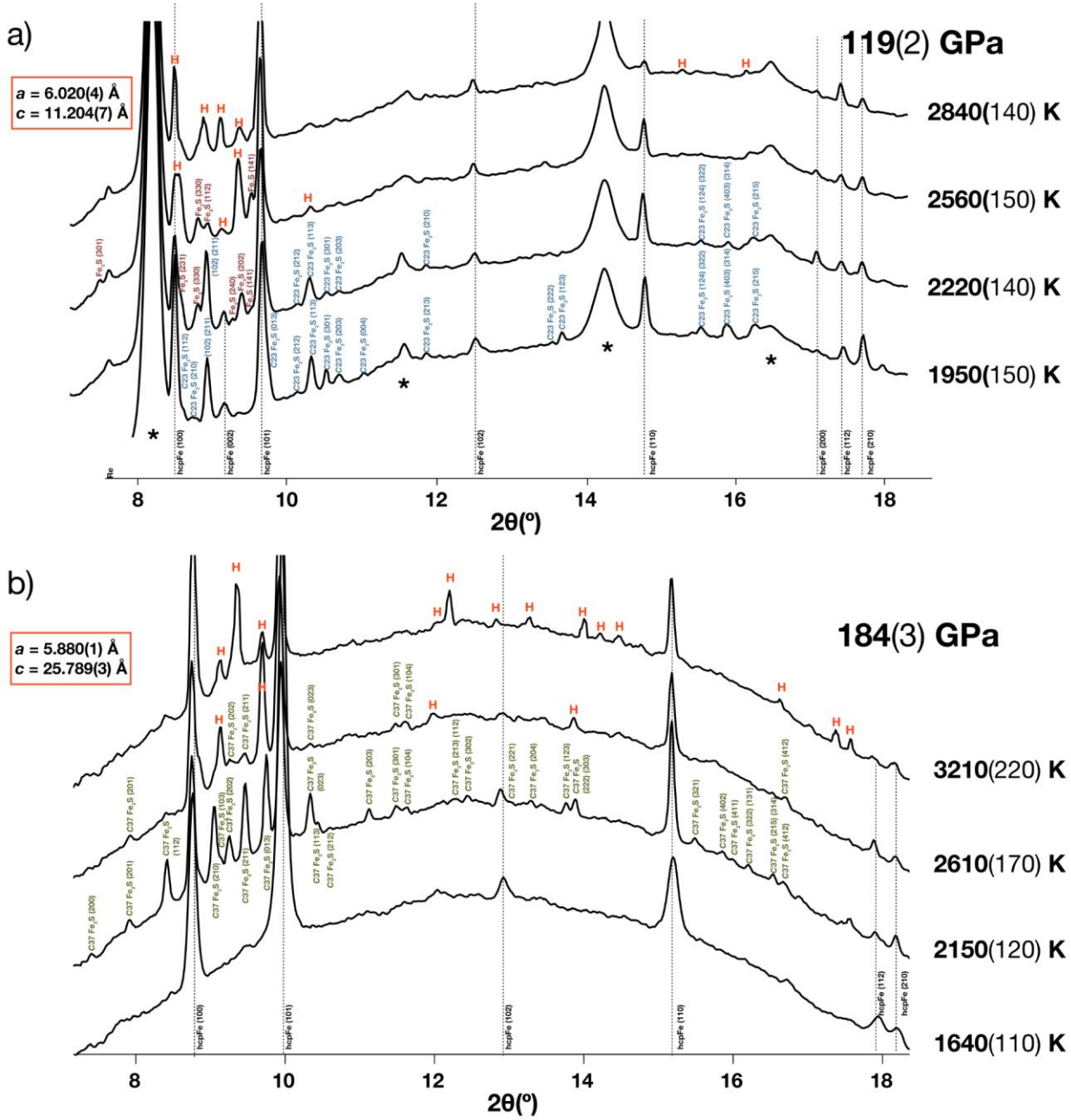

Supplementary Information References

Aronsson, B. (1955) The crystal structure of Ni_3P. (Fe_3P-Type). Acta Chemica Scandinavica, *9*, 137-140.

Blanchard, P.E., Grosvenor, A.P., Cavell, R.G. and Mar, A. (2008) X-ray Photoelectron and Absorption Spectroscopy of Metal-Rich Phosphides M_2P and M_3P (M= Cr− Ni). Chemistry of Materials, 20, 7081-7088.

Chen, J.H. and Whitmire, K.H. (2018) A structural survey of the binary transition metal phosphides and arsenides of the d-block elements. Coordination Chemistry Reviews, 355, 271–327.

El-Boragy, M., Bhan, S. and Schubert, K. (1970) Kristallstruktur von Pd_5Sb_2 und Ni_5As_2 und einigen varianten. Journal of the Less Common Metals, 22, 445–458.

Fei, Y., Li, J., Bertka, C.M. and Prewitt, C.T. (2000) Structure type and bulk modulus of Fe_3S, a new iron-sulfur compound. American Mineralogist, 85, 1830–1833.

Frank, K. and Schubert, K. (1971) Kristallstruktur von $Ni_{31}Si_{12}$. Acta Crystallographica Section B: Structural Crystallography and Crystal Chemistry, 27, 916–920.

Kamada, S., Terasaki, H., Ohtani, E., Sakai, T., Kikegawa, T., Ohishi, Y., Hirao, N., Sata, N. and Kondo, T. (2010) Phase relationships of the Fe–FeS system in conditions up to the Earth's outer core. Earth and Planetary Science Letters, 294, 94–100.

Kamada, S., Ohtani, E., Terasaki, H., Sakai, T., Miyahara, M., Ohishi, Y. and Hirao, N. (2012) Melting relationships in the Fe–Fe_3S system up to the outer core conditions. Earth and Planetary Science Letters, 359, 26–33.

Kjekshus, A., Skaug, K.E., Hebrew, C., Van Buren, C.T., Klæboe, P. and Swahn, C.G. (1973). On the crystal structure of Ni_5As_2. Acta Chem. Scand., 27, 582–588.

Litasov, K.D., Shatskiy, A.F., Minin, D.A., Kuper, K.E. and Ohfuji, H. (2019). The Ni–Ni_2P phase diagram at 6 GPa with implication to meteorites and super-reduced terrestrial rocks. High Pressure Research, 39, 561–578.

Morard, G., Andrault, D., Guignot, N., Sanloup, C., Mezouar, M., Petitgirard, S. and Fiquet, G. (2008). In situ determination of Fe–Fe_3S phase diagram and liquid structural properties up to 65 GPa. Earth and Planetary Science Letters, 620–626.

Mori, Y., Ozawa, H., Hirose, K., Sinmyo, R., Tateno, S., Morard, G. and Ohishi, Y. (2017) Melting experiments on Fe–Fe_3S system to 254 GPa. Earth and Planetary Science Letters, 464 135–141.

Okada, A., Kobayashi, K., Ito, T. and Sakurai, T. (1991) Structure of synthetic perryite, $(Ni, Fe)_8(Si, P)_3$. Acta Crystallographica Section C: Crystal Structure Communications, 47, 1358–1361.

Oryshchyn, S., Babizhetskyy, V., Zhak, O., Stoyko, S., Guérin, R., and Simon, A. (2011) Crystal structure of HT-Ni_5P_2 and reinvestigation of isotypic Ni_5As_2. Intermetallics, 19, 1041–1046.

Ozawa, H., Hirose, K., Suzuki, T., Ohishi, Y. and Hirao, N. (2013) Decomposition of Fe_3S above 250 GPa. Geophysical research letters, 40, 4845–4849.

Rundqvist, S. (1960) The structures of Co_2P, Ru_2P and related phases. Acta Chemica Scandinavica, 14, 1961–1979.

Rundqvist, S. and Jellinek, F. (1959) The structures of Ni_6Si_2B, Fe_2P and some related phases. Acta Chemica Scandinavica, 13, 425–432.

Saini, G.S., Calvert, L.D., and Taylor, J.B. (1964). Compounds of the type M_5X_2: Pd_5As_2, Ni_5Si_2, and Ni_5P_2. Canadian Journal of Chemistry, 42, 1511–1517.

Seagle, C.T., Campbell, A.J., Heinz, D.L., Shen, G. and Prakapenka, V.B. (2006) Thermal equation of state of Fe_3S and implications for sulfur in Earth's core. Journal of Geophysical Research: Solid Earth, 111.

Thompson, S., Komabayashi, T., Breton, H., Suehiro, S., Glazyrin, K., Pakhomova, A. and Ohishi, Y. (2020) Compression experiments to 126 GPa and 2500 K and thermal equation of state of Fe_3S: Implications for sulphur in the Earth's core. Earth and Planetary Science Letters, 534, 116080.

Yokoo, S., Hirose, K., Sinmyo, R. and Tagawa, S. (2019) Melting experiments on liquidus phase relations in the Fe-S-O ternary system under core pressures. Geophysical research letters, 46, 5137–5145.

Zurkowski, C.C., Lavina, B., Chariton, S., Tkachev, S., Prakapenka V.B. and Campbell A.J., *in press*. The crystal structure of Fe_2S at 90 GPa based on single-crystal X-ray diffraction techniques. American Mineralogist, https://doi.org/10.2138/am-2022-7973

Zurkowski, C. C., Lavina, B., Brauser, N. M., Davis, A. H., Chariton, S., Tkachev, S., Greenberg, E., Prakapenka, V. B., and Campbell, A. J., *in press.* Pressure-induced *C*23-*C*37 transition and compression behavior of orthorhombic Fe_2S to Earth's core pressures and high temperatures. https://doi.org/10.2138/am-2022-8187